Simulating the flow of interacting ferrofluids with multiparticle collision dynamics

Patrick Ilg◉

School of Mathematical, Physical, and Computational Sciences, University of Reading, Reading, RG6 6AX, United Kingdom

Ferrofluid flow is fascinating since its fluid properties can conveniently be manipulated by external magnetic fields. Novel applications in micro- and nanofluidics as well as in biomedicine have renewed the interest in the flow of colloidal magnetic nanoparticles with a focus on small-scale behavior. Traditional flow simulations of ferrofluids, however, often use simplified constitutive models and do not include fluctuations that are relevant at small scales. Here we address these challenges by proposing a hybrid scheme that combines the multiparticle collision dynamics method for modeling hydrodynamics with Brownian dynamics simulations of a reliable kinetic model describing the microstructure, magnetization dynamics, and resulting stresses. Since both multiparticle collision dynamics and Brownian dynamics are mesoscopic methods that naturally include fluctuations, this hybrid scheme presents a promising alternative to more traditional approaches, also because of the flexibility to model different geometries and modifying the constitutive model. The scheme was tested in several ways. Poiseuille flow was simulated for various model parameters and effective viscosities were determined from the resulting flow profiles. The effective, field-dependent viscosities are found to be in very good agreement with theoretical predictions. We also study Stokes' second flow problem for ferrofluids. For weak amplitudes and low frequencies of the oscillating plate, we find that the velocity profiles are well described by the result for Newtonian fluids at the corresponding, field-dependent viscosity. Furthermore, the time-dependent profiles of the nonequilibrum magnetization component are well approximated by their steady-state values in stationary shear when evaluated with the instantaneous local shear rate. Finally, we also apply our scheme to simulate ferrofluid shear flow over a rough surface. We find characteristic differences in the nonequilibrium magnetization components when the external field is oriented in flow and in a gradient direction.

I. INTRODUCTION

Colloidal suspensions of magnetic nanoparticles (MNPs) in nonmagnetic carrier fluids—known as ferrofluids—show fascinating flow behavior due to their sensitivity to externally applied magnetic fields [1,2]. Since the apparent viscosity can conveniently be controlled by an external field, these fluids find promising applications ranging from engineering and micro- and nanofluidics to biomedicine [3–6]. Not surprisingly, this exciting field is currently under active research (see, e.g., Refs. [7,8] for recent reviews).

From a theoretical point of view, ferrofluids are a particularly interesting kind of complex fluid where the fluid magnetization comes into play as a slow, nonhydrodynamic variable [9,10]. Similar to other complex fluids, formulating reliable constitutive models for ferrofluids is a formidable challenge. Over the last decades, several different magnetization equations and corresponding constitutive models have been proposed, based on thermodynamic or kinetic theory arguments, but no agreement has been reached yet (see, e.g., Refs. [10–18] and references therein). Some of these constitutive models have been tested in experiments [19,20] or against detailed molecular simulations [21,22]. Despite significant progress in modeling ferrofluids, many flow simulations to date still use rather simple constitutive models, sometimes neglecting the magnetization dynamics altogether [23–27]. Since flow simulations are needed to design and plan technical

applications as well as biomedical treatments, the urgent need for novel methods that are able to implement reliable constitutive models by incorporating the suspension microstructure has been pointed our recently [28].

Here, we address this challenge by extending the multiparticle collision (MPC) approach to ferrofluids that we developed recently [29]. MPC is a very flexible method to simulate fluid flow that naturally includes thermal fluctuations [30–32]. The method has recently been used to include hydrodynamic interaction effects in particle-level simulations of ferrofluids [33]. On a more coarse-grained level, the MPC method has recently been extended to describe the flow of complex fluids such as polymer solutions [34] and nematics [35]. The hybrid MPC scheme proposed for ferrofluids in Ref. [29] couples Brownian Dynamics simulations of a kinetic model of ferrofluids to the MPC flow solver. In the spirit of similar hybrid schemes which simulate complex fluids with stochastic simulations and finite-element flow solvers [36], these methods do not require closed-form constitutive equations. Instead, the stochastic simulations directly solve the underlying kinetic model, thereby avoiding the need for closure approximations. Note that the stochastic simulations include fluctuations in the stress contributions due to the finite size of the ensemble used [36]. In Ref. [29], the classical kinetic model of Martsenyuk *et al.* [13] was implemented using the MPC method. Although this model is widely considered

a reliable representation of ultradilute ferrofluids, the model fails to account for several phenomena observed for real ferrofluids, such as enhanced anisotropy of the magnetoviscous effect [37,38] and sensitivity to nonrotational components of the flow field [20].

The failure of the classical kinetic model to describe these phenomena can be traced back to the neglect of the internal microstructure of ferrofluids. The chain model proposed by Zubarev and Iskakova [14,15] extends the classical kinetic model and thereby overcomes these shortcomings. Rather than considering isolated MNPs, the chain model develops a kinetic theory for the dynamics of rigid, chainlike aggregates of MNPs that are formed due to dipolar interactions among the nanoparticles. Comparison to experiments and to more detailed, many-body molecular simulations of interacting ferrofluids show that the chain model captures the relevant phenomena at least semiquantitatively [16,22,39,40]. Therefore, in the present paper, we extend our previous work [29] by implementing the chain model in a hybrid MPC scheme for ferrofluids. Thereby, we also drop the restriction to two spatial dimensions employed in Ref. [29] and present here a fully three-dimensional scheme that is able to provide a physically sound description of the flow of real ferrofluids. We verify our implementation of the model by quantitatively comparing simulation results for the effective viscosity extracted from Poiseuille flow to analytical results. Using a broad range of model parameters, we find very good agreement between simulation and theoretical results. We also considered Stokes second flow problem for ferrofluids. This benchmark problem considers the flow induced by an infinite flat plate, harmonically oscillating in its plane. Previous studies showed that the MPC method is able to simulate the resulting flow for Newtonian fluids [41]. Here we determine the time-periodic flow profile for ferrofluids and find very good agreement with the prediction for a Newtonian fluid with the corresponding effective, field-dependent viscosity. Finally, we use our hybrid MPC scheme to study ferrofluid shear flow over a rough surface, where the roughness is idealized as square ridges. Such structures are commonly encountered in micropatterned surfaces and in microfluidic devices.

The paper is organized as follows. In Sec. II, we review the equations of ferrofluid hydrodynamics and their coupling to the stochastic formulation of the chain model. In Sec. III, we describe the hybrid MPC model, where we present the coupling of the angular momentum-conserving MPC algorithm with Brownian dynamics simulations of the chain model for ferrofluids. Verification of our implementation of this hybrid scheme is shown in Sec. IV. Results for Stokes second flow problem are shown in Sec. V and ferrofluid shear flow over rough surfaces is presented in Sec. VI. Finally, some conclusions are offered in Sec. VII.

II. FLUCTUATING FERROFLUID HYDRODYNAMICS

We here summarize the basic hydrodynamic equations for ferrofluid dynamics. For more details, the reader is referred to Refs. [9–12]. We start with the fluid momentum balance equation that can be expressed as

$$\rho \frac{d}{dt} \mathbf{v} = -\nabla p + \nabla \cdot \boldsymbol{\sigma}^{\text{hyd}} + \rho \mathbf{f_M}, \quad (1)$$

where ρ denotes the fluid density, $\mathbf{v}$ the velocity field, and d/dt the material derivative. The driving forces are the gradients of the scalar pressure p and the hydrodynamic stress tensor $\boldsymbol{\sigma}^{\text{hyd}}$, as well as the Kelvin-Helmholtz force density $\mathbf{f_M}$. The latter can be written as

$$\rho \mathbf{f_M} = (\mathbf{M} \cdot \nabla)\mathbf{H} + \tfrac{1}{2} \nabla \times (\mathbf{M} \times \mathbf{H}), \quad (2)$$

where $\mathbf{H}$ denotes the magnetic field and $\mathbf{M}$ the magnetization. The Kelvin-Helmholtz force (2) is responsible for much of the peculiarities of ferrofluid flow and vanishes when no external field is applied. As we shall later see, Eq. (2) is the only field-dependent driving force in the case of noninteracting, i.e., ultradilute ferrofluids.

Besides the hydrodynamic balance equations, the fluid also needs to satisfy the magnetostatic Maxwell equations

$$\nabla \cdot (\mathbf{H} + \mathbf{M}) = 0, \quad \nabla \times \mathbf{H} = \mathbf{0}. \quad (3)$$

Equations (1)–(3) are not closed, as they are missing constitutive equations for the stress tensor $\boldsymbol{\sigma}^{\text{hyd}}$ and the magnetization $\mathbf{M}$. There has been some discussion in the literature about the appropriate form of the stress tensor $\boldsymbol{\sigma}^{\text{hyd}}$ and corresponding magnetization equation for interacting ferrofluids (see, e.g., Refs. [10–12,17–20] and references therein). As discussed in Ref. [11], assuming fast rotational relaxation appropriate for ferrofluids implies that the hydrodynamic stress tensor $\boldsymbol{\sigma}^{\text{hyd}}$ is symmetric.

Here, we employ the so-called chain model of ferrofluids [14,15]. In this mesoscopic model, it is assumed that dipolar interactions among the MNPs lead to chainlike aggregates that can be described approximately as rigid ellipsoids of revolution with axis ratio r. The stronger the dipolar interactions, the larger the value of r. The special case $r = 1$ describes spherical particles, corresponding to noninteracting ferrofluids. Within the chain model, one can use the theory of dilute rigid suspensions to find that the stress tensor can be expressed as $\boldsymbol{\sigma}^{\text{hyd}} = \mathbf{T}^{\text{vis}} + \mathbf{T}^{\text{pot}}$, with the viscous contribution [15,42]

$$\mathbf{T}^{\text{vis}} = 2\eta_s \mathbf{D} + 5\eta_s \phi [2Q_1 \mathbf{D} + Q_4 (\mathbf{D} \cdot \mathbf{A}^{(2)} + \mathbf{A}^{(2)} \cdot \mathbf{D}) - Q_5 \mathbf{D} : \mathbf{A}^{(4)}], \quad (4)$$

where ϕ denotes the volume fraction of the ellipsoidal aggregates, η_s the solvent viscosity, and $\mathbf{D} = (1/2)[(\nabla \mathbf{v})^T + \nabla \mathbf{v}]$ the symmetric velocity gradient. The quantities $\mathbf{A}^{(n)}$ denote the nth-order alignment tensors of the ellipsoid orientation and $Q_j = Q_j(r)$, $j = 0, \ldots, 5$, are geometric coefficients that depend solely on the axis ratio r. More details on these quantities are given in Appendix A. In the presence of an interaction potential, as is the case for an externally applied magnetic field $\mathbf{H}$, there is an additional potential contribution to the stress tensor for rigid suspensions. In the rigid-dipole approximation, where the magnetic moment is assumed to remain fixed within the particle and aligned parallel to the symmetry axis of the ellipsoid, this contribution is given by [43]

$$\mathbf{T}^{\text{pot}} = \tfrac{1}{2} n k_B T B [6\mathbf{A}^{(2)} - 2\mathbf{I} - (\mathbf{mh} + \mathbf{hm}) + \mathbf{A}^{(3)} \cdot \mathbf{h}]. \quad (5)$$

In Eq. (5), we introduced the number density n of ellipsoidal aggregates and their shape factor $B = (r^2 - 1)/(r^2 + 1)$. The absolute temperature is denoted by T and k_B is Boltzmann's constant. Moreover, we defined the dimensionless magnetic

field $\mathbf{h} = \mu \mathbf{H}/k_{\mathrm{B}}T$ with μ the magnetic moment of the ellipsoidal aggregate and $h = |\mathbf{h}|$ the Langevin parameter. With the help of the saturation magnetization $M_{\mathrm{sat}} = n\mu$, the reduced magnetization $\mathbf{m}$ is defined by $\mathbf{M} = M_{\mathrm{sat}}\mathbf{m}$. Finally, $\mathbf{I}$ denotes the three-dimensional unit matrix. For the special case of spherical particles, $r = 1$ such that $\mathbf{T}^{\mathrm{pot}} = \mathbf{0}$ and $\mathbf{T}^{\mathrm{vis}} = 2\eta_{\mathrm{s}}[1 + 5\phi/2]\mathbf{D}$ reduces to the well-known expression for a dilute suspension of hard spheres.

Having specified the stress tensor $\boldsymbol{\sigma}^{\mathrm{hyd}}$, a constitutive model for the magnetization dynamics and corresponding higher-order alignment tensors is still needed to close the system of Eqs. (1)–(5). Within the chain model, this is done via a stochastic description for the rotational motion $\frac{d}{dt}\mathbf{u} = \boldsymbol{\omega} \times \mathbf{u}$ of the orientation $\mathbf{u}$ of the ellipsoidal aggregates. Thanks to the rigid-dipole approximation, $\mathbf{u}$ coincides with the direction of the magnetic moment of the aggregate. Therefore, the magnetization and higher-order moments can be derived as expectation values, $\mathbf{m} = \langle \mathbf{u} \rangle$. The angular velocity $\boldsymbol{\omega}$ of the ellipsoidal aggregate can be obtained from the balance of hydrodynamic, magnetic, and Brownian torques,

$$\boldsymbol{\omega} = \boldsymbol{\Omega} + B\mathbf{u} \times \mathbf{D} \cdot \mathbf{u} + \frac{\mu}{\xi}\mathbf{u} \times \mathbf{H} + \mathbf{R}, \qquad (6)$$

where $\boldsymbol{\Omega} = (1/2)\nabla \times \mathbf{v}$ denotes the local vorticity of the flow and ξ the rotational friction coefficient of the ellipsoidal aggregate. The Gaussian random torques $\mathbf{R}$ vanish on average, $\langle \mathbf{R} \rangle = \mathbf{0}$, and satisfy $\langle \mathbf{R}(t)\mathbf{R}(t')\rangle = \frac{2k_{\mathrm{B}}T}{\xi}\delta(t - t')\mathbf{I}$ [44].

It should be noted that the original chain model considers a distribution of chain lengths. For simplicity, we here consider a single aspect ratio only that can be interpreted as representing a typical chain length [43]. Since chains are assumed to be noninteracting [15], it is straightforward to extend the present paper by including a distribution of aspect ratios. Furthermore, we mention that the chain model in the form presented here disregards flow-induced changes in chain lengths. Therefore, we consider in the following relatively weak flows and moderate chain lengths where these effects are known to be weak [22,38]. This paper can be extended by including phenomenological relations for a reduction of mean chain lengths in flow (see, e.g., [16,39] and references therein).

III. FERROHYDRODYNAMIC MPC MODEL

We now describe the hybrid model combining MPC and Brownian dynamics to simulate fluctuating ferrohydrodynamics of interacting ferrofluids. While the original MPC method was designed for simple liquids [30,31], recent years have seen several extensions of the method to complex fluids [32] such as polymer solutions [34] and nematics [35]. Very recently, we have proposed to model fluctuating ferrohydrodynamics with the help of MPC [29]. In this model, each MPC particle represents a small fluid element, carrying its individual magnetic moment. The particles' magnetic moments perform stochastic rotational dynamics in the presence of local magnetic fields and velocity gradients. The additional Kelvin-Helmholtz force entering the fluid momentum balance equation leads to backflow effects. This model and its implementation have been validated in Ref. [29] for two dimensions and for a constitutive model that is appropriate for ultradilute

(noninteracting) ferrofluids only. Here we want to extend the model proposed in Ref. [29] to three spatial dimensions and also generalize the constitutive model used there to include also interacting ferrofluids, which show a richer anisotropic behavior and enhanced viscoelastic effects compared to their noninteracting counterparts [16].

Within the MPC method, the fluid is represented as a collection of N particles at positions $\mathbf{r}_i$ with velocities $\mathbf{v}_i$ and masses $m_i = m$ with $i = 1, \ldots, N$. In a coarse-grained description, each particle represents a small volume of fluid with magnetic moment $\mu \mathbf{u}_i$, where $\mathbf{u}_i$ is a three-dimensional unit vector and μ the magnitude of the magnetic moment, assumed to be identical for all particles. The basic idea behind the MPC method is that relatively simple dynamic rules for these particles are sufficient to reproduce hydrodynamic behavior on slightly larger length and longer time scales, provided that mass, momentum and energy is conserved locally.

In particular, the MPC method splits the dynamics into a streaming and a collision step that we describe next. In the streaming step, particle positions and velocities are updated over a time interval Δt according to [45]

$$\mathbf{r}_i(t + \Delta t) = \mathbf{r}_i(t) + \Delta t\, \mathbf{v}_i(t) + \frac{\Delta t^2}{2m}\mathbf{F}_i(t), \qquad (7)$$

$$\mathbf{v}'_i(t) = \mathbf{v}_i(t) + \frac{\Delta t}{m}\mathbf{F}_i(t), \qquad (8)$$

with $\mathbf{F}_i(t)$ the total force acting on particle i at time t. In view of Eq. (1) and modeling an applied pressure gradient as external force, $\mathbf{f}_{\mathrm{ext}} = -\rho^{-1}\nabla p$, we can identify the force acting on the MPC particles as

$$\mathbf{F}_i = \mathbf{f}_{\mathrm{ext}} + \mathbf{f}_{\mathbf{M}}(\mathbf{r}_i) + \frac{1}{\rho}\nabla \cdot \boldsymbol{\sigma}^{\mathrm{hyd}}(\mathbf{r}_i). \qquad (9)$$

To exchange momentum between particles, the streaming step is followed by a collision step. Different collision rules for MPC algorithms have been proposed that conserve mass and momentum. Here, since we are interested in the rotational dynamics, we choose the so-called Andersen-AR+a thermostat, which performs collisions that additional preserve angular momentum [46]. A peculiarity of MPC schemes is that they do not resolve individual collisions between particles but perform collisions simultaneously on all particles currently residing in the same collision cell. To this end, we divide the total system into $N_x \times N_y \times N_z$ cubic collisions cells of linear size a. We denote with $\mathbf{v}'_i$ the velocity of particle i at time t after the streaming step (8). The center-of-mass velocity of cell C_i to which particle i belongs at this instance is $\mathbf{V}_{C_i} = N_{C_i}^{-1}\sum_{j \in C_i} \mathbf{v}'_j$. Collisions and thermostatting are done simultaneously in the Andersen-AT+a algorithm by assigning new velocities to all particles in the same collision cell C_i according to

$$\mathbf{v}_i(t + \Delta t) = \mathbf{V}_{C_i} + \hat{\mathbf{v}}_i^{\mathrm{MB}} + \mathbf{O}_{C_i} \times \mathbf{r}_{i,c}, \qquad (10)$$

where $\hat{\mathbf{v}}_i^{\mathrm{MB}} = \mathbf{v}_i^{\mathrm{MB}} - N_{C_i}^{-1}\sum_{j \in C_i} \mathbf{v}_j^{\mathrm{MB}}$ and $\mathbf{v}_i^{\mathrm{MB}}$ is a random velocity vector drawn from the three-dimensional Maxwell-Boltzmann distribution with zero mean and standard deviation $\sqrt{k_{\mathrm{B}}T/m}$. The last term in Eq (10) removes angular momentum introduced by the random velocities,

$$\mathbf{L}_{C_i} = m \sum_{j \in C_i} \mathbf{r}_{j,c} \times (\mathbf{v}'_j - \mathbf{v}_j^{\mathrm{MB}}), \qquad (11)$$

with $\mathbf{O}_{C_i} = \mathbf{I}_{C_i}^{-1} \cdot \mathbf{L}_{C_i}$ and $\mathbf{I}_{C_i}$ the moment of inertia tensor of this collision cell, $\mathbf{I}_{C_i} = m \sum_{j \in C_i} [r_{j,c}^2 \mathbf{I} - \mathbf{r}_{j,c} \mathbf{r}_{j,c}]$, where $\mathbf{r}_{i,c} = \mathbf{r}_i - \mathbf{r}_{\mathrm{cm}}$ the position of particle i relative to the center of mass of its collision cell. Note that the positions $\mathbf{r}_i$ in Eqs. (10) and (11) are understood to denote the current positions $\mathbf{r}_i(t + \Delta t)$ after the streaming step Eq (7). In order to avoid problems due to the violation of Galilean invariance arising from using a fixed grid of collision cells, we follow common practice [31] and shift the grid by a three-dimensional vector, where each component is randomly drawn from a uniform distribution in $[-a/2, a/2]$.

In addition to the translational motion (7), (8), and (10), we also need to specify the rotational motion associated with the magnetic moment of the particles. As mentioned in Sec. II, we here employ the so-called chain model of ferrofluids [15], where interactions between MNPs are assumed to lead to rigid, chainlike aggregates that can be represented as rigid ellipsoids of revolution with axis ratio r. Assuming furthermore that the magnetic moments are rigidly fixed within the particles, the magnetization dynamics is slaved to the rotational dynamics of the aggregate. For the latter, a weak first-order scheme to integrate Eq. (6) reads $\Delta \mathbf{u}_i = \Delta \boldsymbol{\omega}_i \times \mathbf{u}_i(t)$ with

$$\Delta \boldsymbol{\omega}_i = \left[\boldsymbol{\Omega}_{C_i} + B \mathbf{u}_i \times \mathbf{D}_{C_i} \cdot \mathbf{u}_i + \frac{1}{2\tau_{\mathrm{B}}} \mathbf{u}_{C_i} \times \mathbf{h}_i \right] \Delta t_{\mathrm{BD}} + \Delta \mathbf{W}_i, \tag{12}$$

where $\Delta \mathbf{W}_i$ denotes a three-dimensional Wiener increment over the time interval Δt_{BD}, while $\boldsymbol{\Omega}_{C_i}$, $\mathbf{D}_{C_i}$ and $\mathbf{h}_{C_i}$ denote the vorticity $\boldsymbol{\Omega}$, the symmetric velocity gradient $\mathbf{D}$, and the dimensionless local field $\mathbf{h}$, respectively, evaluated at the center of the collision cell to which particle i belongs to. In Eq. (12), we have also introduced the Brownian rotational relaxation time $\tau_{\mathrm{B}} = \xi / (2 k_B T)$.

The time step Δt_{BD} for the Brownian dynamics scheme (12) does not need to be identical to the time step Δt of the MPC steps (7)–(10). In MPC, the time step Δt can typically be chosen rather large, while stochastic algorithms such as Eq. (12) require $\Delta t_{\mathrm{BD}} / \tau_{\mathrm{B}}$ to be small. Here, we use $\Delta t_{\mathrm{BD}} = \Delta t / n_{\mathrm{BD}}$ and perform n_{BD} steps of Brownian dynamics simulations (12) for fixed values of $\boldsymbol{\Omega}_{C_i}$, $\mathbf{D}_{C_i}$, and $\mathbf{h}_{C_i}$ for every step of MPC. In practice, we use a second-order stochastic Heun scheme with (12) as a predictor step, which allows us to use larger time steps Δt_{BD}, leading to moderate values of n_{BD} and consequently a rather efficient scheme.

The velocity gradients needed to calculate $\boldsymbol{\Omega}_{C_i}$ and $\mathbf{D}_{C_i}$ we compute from finite-difference schemes of the velocity field $\mathbf{v}(\mathbf{r}, t)$. The latter we obtain from the particles' velocities $\mathbf{v}_i$ via kernel smoothing, $\mathbf{v}(\mathbf{r}, t) = \bar{K}^{-1} \sum_{i=1}^{N} \mathbf{v}_i(t) K(|\mathbf{r} - \mathbf{r}_i(t)|)$ with $\bar{K} = \sum_{j=1}^{N} K(|\mathbf{r} - \mathbf{r}_j(t)|)$ and K the Epanechnikov kernel. More details can be found in Ref. [29]. Finally, we need to calculate the additional magnetic driving forces in the momentum balance, i.e., the Kelvin-Helmholtz force (2) and the divergence of the extra stress tensor, Eqs. (4) and (5). Also for these quantities, we use kernel smoothing methods to compute the fields $\mathbf{m}$, $\mathbf{h}$, $\mathbf{A}^{(k)}$ and finite-difference schemes to calculate their spatial gradients. The simulations discussed below employ periodic as well as no-slip boundary conditions. In the flow and vorticity direction, we use periodic boundary conditions, while no-slip conditions are employed at channel

and obstacle walls. In MPC, no-slip boundary conditions are conveniently implemented by the bounce-back rule for particle's positions and velocities. We also add temporary ghost particles for the collisions in underpopulated boundary cells [45]. An overview of the resulting algorithm is given in Appendix B.

IV. VALIDATION AND RESULTS FOR CHANNEL FLOW

We have implemented and tested the ferrohydrodynamic MPC model described in Sec. III for systems of different sizes $L_x \times L_y \times L_z$, ranging from $20 \times 20 \times 20$ to $50 \times 50 \times 10$ and $100 \times 25 \times 5$. Following common practice, we choose the linear size a of the collision cell as unit length, $a = 1$. Therefore, the lengths L_x, L_y, L_z are equal to the number of collision cells in these directions, N_x, N_y, N_z, respectively. With $Q = \langle N_{C_i} \rangle$ the average number of particles per collision cell, each simulation contains a total number of $N = Q N_x N_y N_z$ MPC particles.

First, we check the correct implementation of the Andersen-AT+a thermostat. We verified that the angular momentum is indeed conserved in each collision cell. Next, using a system of size 20^3 and applying periodic boundary conditions in all three dimensions, we study the self-diffusion coefficient D_s of the pure MPC fluid. The pure MPC fluid is obtained in this scheme for the special case of setting the number density $n = 0$, thereby switching off magnetic contributions to hydrodynamics since in this case $\mathbf{T}^{\mathrm{pot}} = \mathbf{f}_{\mathbf{M}} = \mathbf{0}$ and $\mathbf{T}^{\mathrm{vis}} = 2\eta_s \mathbf{D}$. Analyzing the particles' mean-squared displacements $\langle \Delta \mathbf{r}_i^2(t) \rangle$, we find a linear relation $\langle \mathbf{r}_i^2(t) \rangle = 6 D_s t$ from which we determine D_s. Good agreement of our simulation results with the theoretical prediction $D_s = (k_B T \Delta t / m)[Q/(Q-2) - 1/2]$ is seen in Fig. 1(a) for large enough Q, for which the theoretical result was derived [46].

We also checked the viscosity coefficients of the pure MPC fluid. To extract viscosity coefficients, we simulate Poiseuille flow in a three-dimensional planar channel for given constant external force f_{ext} driving the flow. No-slip boundary conditions on the channel wall and periodic boundary conditions in the flow and vorticity direction are employed. From the resulting parabolic velocity profile,

$$v_x(y) = \frac{f_{\mathrm{ext}}}{2\nu} y (L_y - y), \tag{13}$$

where L_y denotes the channel height, we determine the kinematic viscosity ν. We perform simulations for a range of different parameter values. Typically, for each of the chosen set of parameters, we employ 10^5 MPC time steps and use the second half to extract average quantities such as the mean velocity profile $v_x(y)$. We fit the numerically determined flow profiles to Eq. (13) to determine the kinematic viscosity ν. Some results for the kinematic viscosity obtained from these fits are shown in Fig. 1(b) versus the time step Δt for two different temperatures T. Different channel geometries were found to lead to the same results within numerical accuracy. The average number of MPC particles per collision cell was chosen as $Q = 20$, which is large enough so the theoretical result [46]

$$\nu_s = \frac{k_B T \Delta t}{m} \left(\frac{Q}{Q - 5/4} - \frac{1}{2} \right) + \frac{a^2}{24\Delta t} \frac{Q - 7/5}{Q} \tag{14}$$
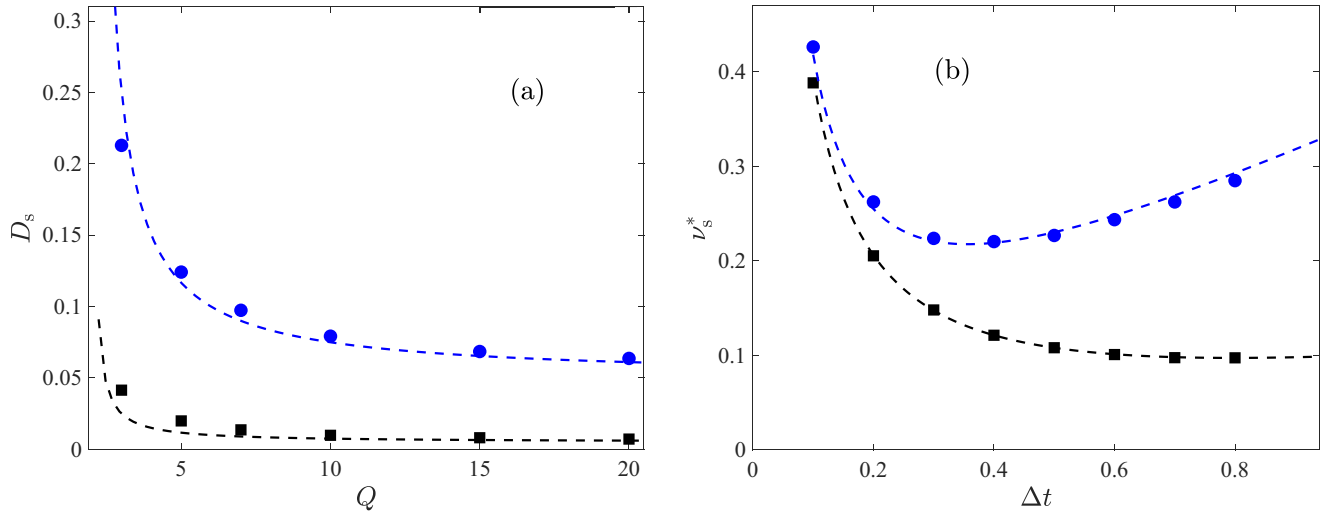
FIG. 1. Transport coefficients of the pure MPC fluid ($n = 0$). (a) Self-diffusion coefficient D_s as a function of mean number of particles per collision cell Q. Lower data correspond to $\Delta t = 0.1$, upper to $\Delta t = 1.0$. Symbols denote the results of MPC simulations, while dashed lines show the theoretical result mentioned in the text. (b) Kinematic viscosity ν_s^* as a function of time step Δt for $Q = 20$ and $T = 0.1$ (lower) and $T = 0.5$ (upper) for the MPC fluid. Dashed lines show the theoretical result Eq. (14).

should apply. Indeed, we find from Fig. 1(b) a good agreement of Eq. (14) with our numerical results. The dimensionless kinematic viscosity is defined as $\nu_s^* = (\Delta t/a^2)\nu_s$. Furthermore, we observe that our numerical results for ν_s are independent of the value f_{ext} of the driving force up to $f_{\text{ext}} = 0.005$. For values $f_{\text{ext}} = 0.005$ and larger, we find that the kinematic temperature is slightly higher than the one imposed by the thermostat. Therefore, if not stated explicitly otherwise, we use the value $f_{\text{ext}} = 0.002$, for which this problem is remedied.

Having tested the pure MPC fluid, we now consider finite concentrations of MNPs, modeled by nonzero values of the number density n. In the absence of an external magnetic field, we expect a viscosity increase known from the theory of rigid suspensions, $\eta_0 = (1 + c_r \phi)\eta_s$, where η_s denotes the viscosity of the solvent fluid, ϕ the volume fraction, and c_r a geometric coefficient given by $c_r = 5Q_1 + 2Q_3 - Q_2$ [42]. The corresponding dimensionless zero-field kinematic viscosity $\nu_0^* = \Delta t/(\rho a^2)\eta_0$ can be expressed as

$$\nu_0^* = \nu_s^* + n^* \tau_B^* \frac{c_r}{3\varphi_r}, \tag{15}$$

where ν_s^* denotes the dimensionless kinematic viscosity of the pure MPC fluid, given by Eq. (14). In Eq. (15), we introduced the quantity $\varphi_r = 5Q_0/(3B)$, which equals 1 for spheres. For spherical particles, $r = 1$, the expression for η_0 reduces to Einstein's famous result with $c_1 = 5/2$. Figure 2 shows the kinematic viscosity in the absence of external fields, obtained from fits of the velocity profile in Poiseuille flow to Eq. (13) for $Q = 30$, $\tau_B^* = 10$, $\Delta t = 0.2$. Very good agreement with the theoretical expression Eq. (15) is found.

Having checked that we find the correct model behavior in the absence of externally applied magnetic fields, we now investigate the magnetoviscous effect, i.e., the field-induced changes of the effective viscosity due to external magnetic fields [16]. We consider dimensionless external fields $\mathbf{h}_0 = \mu\mathbf{H}_0/k_B T$ that are oriented either in flow (x), gradient (y),

or vorticity (z) direction. We first disregard demagnetization effects such that the internal field $\mathbf{H}$ is identical to $\mathbf{H}_0$ and thus $\mathbf{h} = \mathbf{h}_0$. Since we consider planar channel geometries, we expect spatially uniform behavior in flow and vorticity directions and therefore report flow, magnetization and stress profiles in gradient direction only.

Figure 3 shows flow and stress profiles for Poiseuille flow with uniform external force $f_{\text{ext}} = 0.002$ and applied magnetic fields with strengths $h = 0, 2, 5$, respectively, applied in the gradient direction. The axis ratio was chosen as $r = 2$ and the remaining model parameters are $Q = 30$, $T = 0.1$, $n^* = 0.01$, and $\tau_B^* = 10$. Error bars are no larger than the symbol size. Data are shown for a channel with dimensions
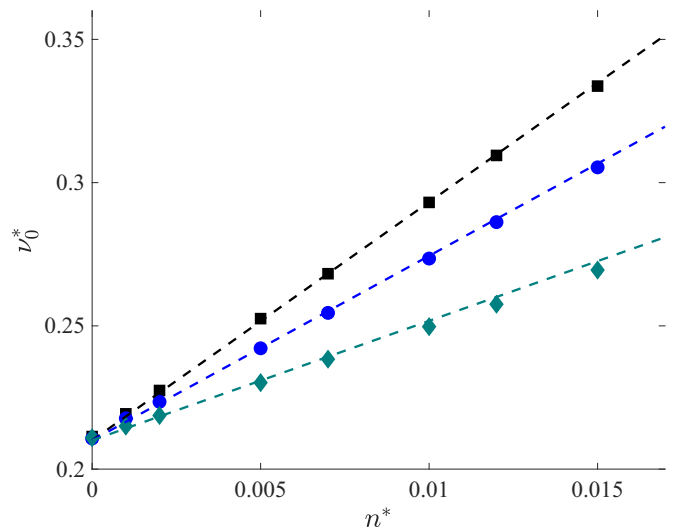

FIG. 2. Kinematic zero-field viscosity ν_0^* as a function of reduced number density n^*. Black, blue, and green symbols correspond to simulation results for axis ratios $r = 1.0, 2.0$, and 5.0, respectively. Dashed lines show the theoretical result (15).
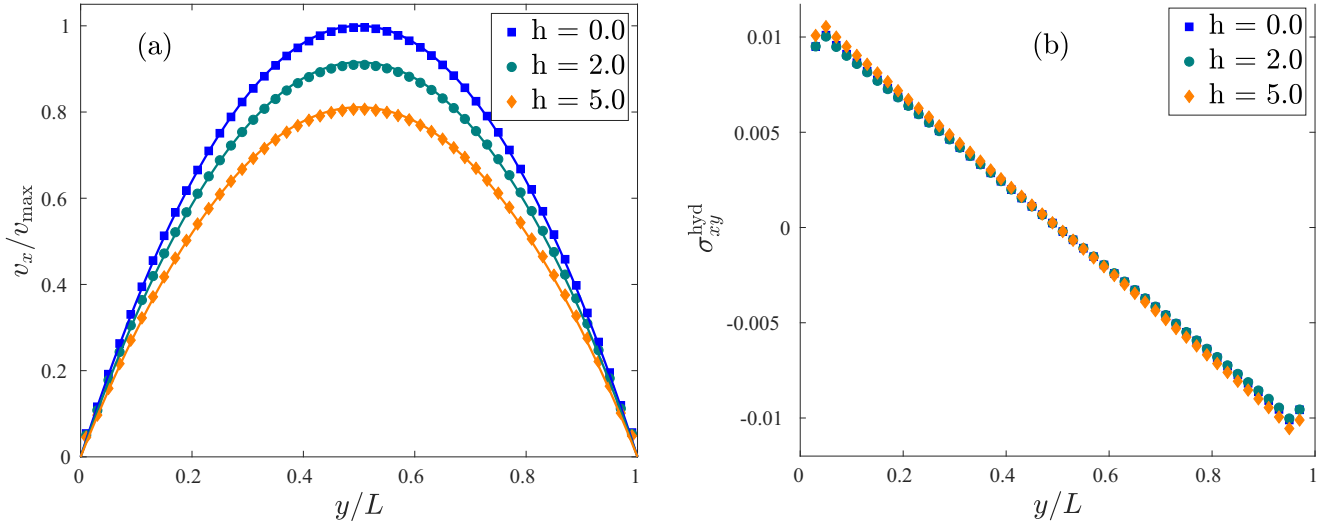
FIG. 3. Profiles of the scaled flow velocity v_x/v_{max} in (a) and the hydrodynamic stress σ_{yx}^{hyd} in (b) across the channel height y. A magnetic field was applied in gradient direction of the flow. Square, circles, and diamonds correspond to a magnitude $h = 0, 2, 5$ of the field, respectively.

$50 \times 50 \times 10$, but results for other dimensions were found identical within statistical uncertainties. For all parameter values investigated, we find nicely parabolic velocity profiles without wall slip. For the parameters used here, the maximum shear rate is around 0.1, corresponding to Peclet numbers of order 1, so shear thinning effects should be weak. The hydrodynamic stress σ_{yx}^{hyd} shows a linear variation across the channel, as expected for laminar flow. We note some deviation from the linear profile very close to the wall.

Fitting again the velocity profiles to Eq. (13), we determine effective, field-dependent viscosity coefficient $v_i^*(h)$. For $\mathbf{h} \to 0$, we recover the zero-field viscosity v_0^* obtained earlier. We observe that the effective viscosity coefficients change as the strength and orientation of the applied field changes. This phenomenon is known as the magnetoviscous effect [9]. Figure 4 shows the result of the simulations, where we find $v_2 > v_1 > v_3$, the expected ordering for elongated particle suspensions [44]. For convenience, we show the viscosity changes $\Delta v_i^* = v_i^*(h) - v_0^*$ relative to their zero-field value.

Within the so-called effective-field approximation (EFA), the viscosity coefficients v_i, $i = 1, 2, 3$ can be calculated analytically [43]. Their explicit expressions are given in Eqs. (A3)–(A5) in Appendix A and are shown in Fig. 4 as dashed lines for the corresponding parameters. We find very good agreement between the numerically determined viscosities and the theoretical results based on the EFA approximation. The agreement is of similar quality as found in planar shear flow [43], once again verifying the implementation and indicating negligible wall slip in the Poiseuille flow considered here.

We now revisit the study of the magnetoviscous effect, this time taking into account demagnetization effects. We apply a spatially homogeneous external magnetic field $\mathbf{H}_0$ outside the channel. Inside the channel, the magnetostatic Maxwell equations (3) require that the internal field $\mathbf{H}$ satisfies $\nabla \cdot \mathbf{H} = -\nabla \cdot \mathbf{M}$. Due to translational invariance of the channel geometry in x and z directions, this relation simplifies to $\partial H_y/\partial y = -\partial M_y/\partial y$. Using, in addition the continuity

conditions of the fields at the channel walls, we find that the internal field is given by $H_x = H_{0,x}$, $H_y = H_{0,y} - M_y$, and $H_z = H_{0,z}$. In terms of the dimensionless magnetic field $\mathbf{h}$, this relation can be written as $h_y = h_{0,y} - 3\chi_L m_y$, where $\chi_L = n\mu^2/(3k_BT)$ denotes the Langevin susceptibility. Disregarding demagnetization effects is therefore justified for small χ_L. In principle, χ_L is not an additional model parameter. If we interpret the axis ratio r of the ellipsoidal aggregate as a proxy for the mean number $\langle n_{ch} \rangle$ of MNPs in a chainlike aggregate, χ_L can approximately be inferred for given r and concentration n (or volume fraction ϕ) via theoretical estimates or from detailed, particle-based computer simulations [16]. Since these estimates come with considerable uncertainties, we here choose values of $\chi_L = 1$ and $\chi_L = 2$ to illustrate
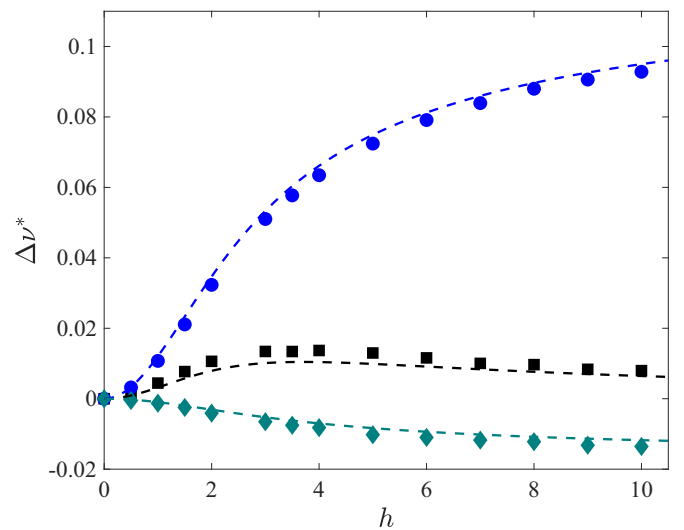

FIG. 4. Dimensionless viscosity change Δv_i^* as function of magnetic field strength h for $r = 2.0$. From top to bottom, the ordering is $i = 2, 1, 3$, i.e., the field is oriented in gradient, flow, and vorticity directions, respectively. The same parameters as in Fig. 3 are chosen.
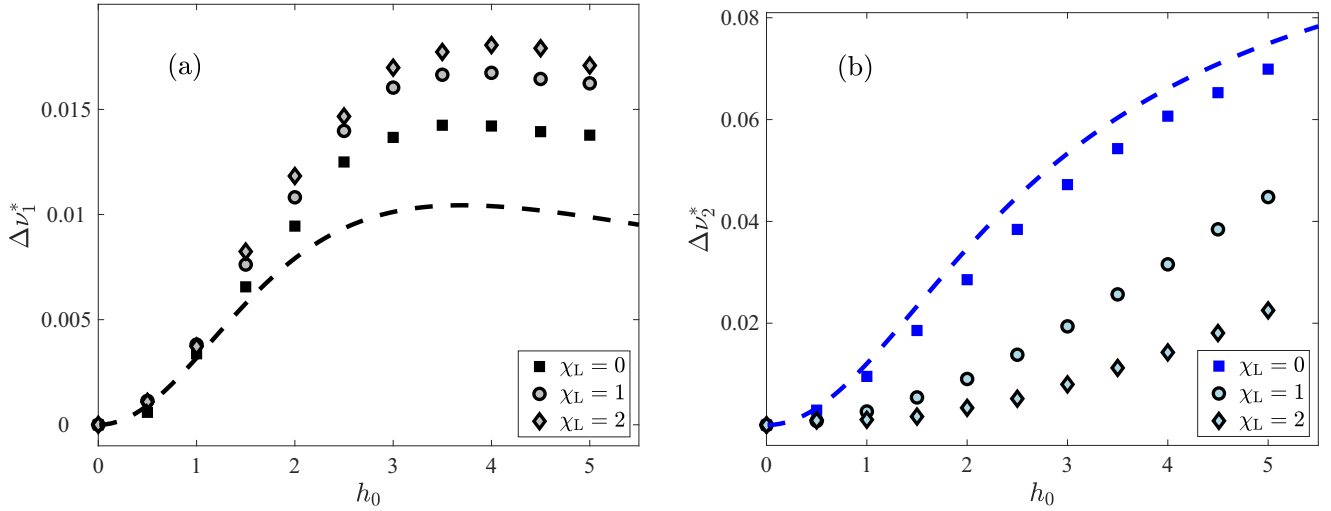
FIG. 5. Dimensionless viscosity change $\Delta\nu_i^*$ as function of externally applied magnetic field of strength h_0 oriented in flow [(a), $i = 1$] and gradient [(b), $i = 2$] directions, respectively. The square symbols correspond to the conditions in Fig. 4 with $h = h_0$, whereas circles and diamonds show the results when demagnetization effects are taken into account using $\chi_L = 1$ and $\chi_L = 2$, respectively.

demagnetization effects for moderate chain-forming ferrofluids with $r = 2$. As can be seen from Fig. 5, demagnetization effects do significantly alter the values of the effective viscosities. In particular, at intermediate field strengths, we find that the value of ν_2 is significantly reduced. Note that the result shown in Fig. 4 still holds in this case, since results are shown as a function of the internal field h, not the externally applied field h_0. We note that the simulation results obtained here are also in qualitative agreement with recent experiments on a magnetite-based commercial ferrofluid in parallel-plate and capillary viscosimeter [39]. Although the model parameters used here are not adequate for the ferrofluid used in these experiments, qualitatively similar behavior is found, such as $\Delta\nu_2^*$ being much larger than $\Delta\nu_1^*$ and increasing over a range of moderate field strengths, whereas $\Delta\nu_1^*$ was found to level off.

V. STOKES SECOND PROBLEM FOR FERROFLUIDS

We now investigate the MPC method for ferrofluids subject to an unsteady, periodic flow. Here, the flow is driven by an infinite planar plate that oscillates harmonically with angular frequency ω in its plane (defined by $y = 0$). Determining the resulting flow profile $v_x(y, t)$ of the unbounded fluid above the plate is known as Stokes second problem [41].

The momentum balance Eq. (1) for the one-dimensional velocity profile reads

$$\frac{\partial v_x}{\partial t} = \frac{1}{\rho}\frac{\partial \sigma_{yx}^{\text{hyd}}}{\partial y} + f_{\mathbf{M},x}, \qquad (16)$$

with the hydrodynamic stress tensor $\sigma_{yx}^{\text{hyd}} = T_{yx}^{\text{vis}} + T_{yx}^{\text{pot}}$. Explicit expressions for these quantities are provided in Appendix C. In the absence of an external magnetic field, Eq. (16) can be rewritten in the familiar form

$$\frac{\partial v_x}{\partial t} = \nu_{\text{eff}}\frac{\partial^2 v_x}{\partial y^2}, \qquad (17)$$

with an effective kinematic viscosity coefficient ν_{eff}. When external magnetic fields are applied, additional spatial gradient terms appear, see Appendix C. For the special case of spatially homogeneous magnetic fields and resulting homogeneous magnetization, Eq. (16) can again be written in the form (17), this time with an effective, frequency- and field-dependent viscosity coefficient ν_{eff}. For zero frequency, explicit expressions for the viscosity coefficients for the chain model are given in Appendix A. Approximate expressions for the corresponding frequency-dependent viscosity coefficients can be found in Ref. [43].

The analytical solution to Stokes second flow problem (17) for the boundary condition $v_x(0, t) = U_0 \cos(\omega t)$ reads

$$v_x(y, t) = U_0 e^{-ky} \cos(\omega t - ky), \qquad (18)$$

with the effective damping parameter $k = \sqrt{\omega/2\nu_{\text{eff}}}$. For Newtonian fluids, it has been verified [41] that the MPC method recovers the exact solution (18) rather well for not too high frequencies ($\omega \lesssim 0.1$).

Here we use the MPC method proposed above to study Stokes second flow problem for ferrofluids. Although the flow is two-dimensional, we have solved the problem in a three-dimensional domain of size $30 \times 30 \times 5$ with periodic boundary conditions applied in x and z directions. For computational convenience, we use a fixed height $L_y = 30a$ with reflecting boundary conditions rather than an infinite size in the perpendicular direction. At the moving plate (i.e., for $y = 0$), we use no-slip boundary conditions via the bounce-back rule as described in Sec. III. To remain within the weak perturbation regime, we follow Ref. [41] and choose the velocity amplitude $U_0 = 0.1$. Further model parameters are chosen as $Q = 30$, $T = 0.1$, $n^* = 0.05$, $\tau_{\text{B}}^* = 10$, $r = 5$ and $\Delta t = 0.2$. With an applied frequency of $\omega = 0.0209$ and kinematic viscosities in the range $\nu_{\text{eff}} \approx 0.4 \ldots 0.8$, this translates to $L_y \approx 3.5 \ldots 5k^{-1}$. To investigate possible finite-size effects, we additionally performed several simulations with $L_y = 50a$. Only minor differences were found. The frequency ω of the oscillating plate is small enough for the MPC method to
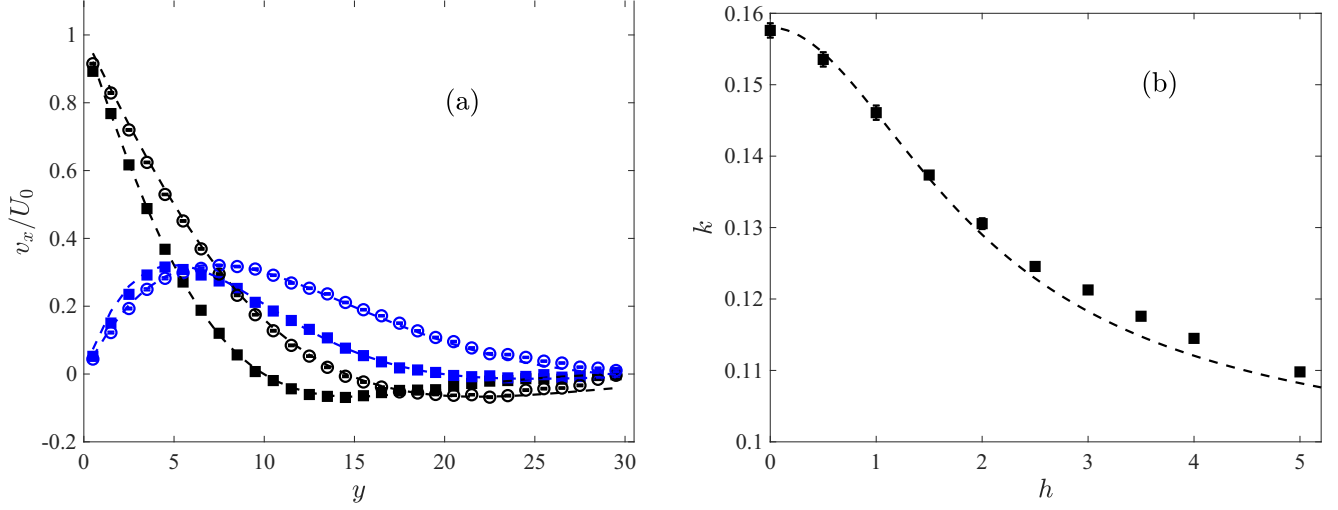
FIG. 6. (a) Flow profile $v_x(y, t)$ for second Stokes problem at times $t = nT_\omega$ (black) and $t = (n + 1/4)T_\omega$ (blue symbols) for an applied field in the vertical direction of strength $h = 0$ (filled) and $h = 5$ (open symbols). Dashed lines show the analytical solution (18), where the damping parameter k is calculated with the corresponding viscosities (A5) for the chain model. (b) Effective damping parameter k as a function of applied field strength h for the same conditions as in (a). Symbols denote results of fits of the profiles from simulations to Eq. (18), dashed line shows the analytical result within the EFA for the chain model.

reproduce the hydrodynamic solution [41]. The velocity profile is averaged over times $t_j = (n + j/4)T_\omega$ with $j = 0, 1, 2$ fixed, where the oscillation period is given by $T_\omega = 2\pi/\omega \approx 300.6$. Averages are accumulated only after $t > 3T_\omega$ to ensure that initial transients have decayed. To reduce statistical uncertainties, we average the profiles over more than 100 oscillation periods.

Figure 6(a) shows the resulting velocity profile $v_x(y, t_j)$, decaying as the distance to the oscillating plate increases. A magnetic field of strength h was applied perpendicular to the oscillating plate. Two time points t_j within the oscillating period, $j = 0$ and $j = 1$, are shown. Also shown in Fig. 6(a) are the analytical profiles (18), where the effective damping parameter k is calculated using the expression (A5) for the steady-state viscosity of the chain model. Very good agreement between MPC simulations and the theoretical results is found.

The pronounced viscosity increases when a magnetic field of dimensionless strength $h = 5$ is applied in the gradient direction compared to the field-free case that we saw in Fig. 4 is mirrored here in a decrease of the effective damping parameter k. We determine the damping parameter k from fits of the simulated velocity profile in Fig. 6(a) to the analytical expression (18). In Fig. 6(b), we show the resulting damping parameter versus the strength of the applied field h in the perpendicular direction. As expected, the effective damping parameter k decreases with increasing field strength h. We also plot the theoretical prediction for k calculated with the result (A5) for the chain model. Again, we find very good agreement between the numerical results and the prediction based on the EFA of the chain model.

In the presence of an applied field perpendicular to the plate, the periodic shearing motion induces a nonequilibrium magnetization component in flow direction. Figure 7 shows the profiles of the magnetization component in flow direction, M_x, normalized with the saturation magnetization M_{sat}. The

same conditions as in Fig. 6 are chosen. Since the induced velocity decays strongly with the distance to the oscillating plate, also the nonequilibrium magnetization component M_x quickly decays to zero for large enough distances. We can rationalize the nonequilibrium magnetization profiles using again the EFA for the chain model. Since the oscillating frequency ω is low, we can use the result for the steady-state nonequilibrium magnetization (C6) and evaluate the expression for the instantaneous local shear rate $\partial v_x/\partial y$. Dashed lines in Fig. 7 show that these assumptions give a good approximation to the numerical data. We note that numerical
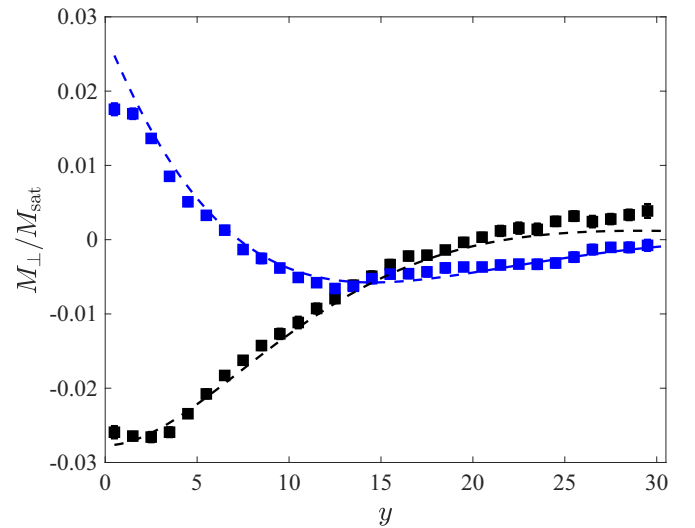

FIG. 7. The relative magnetization component in flow direction is shown as a function of distance to the oscillating plate. A magnetic field of strength $h = 5$ was applied perpendicular to the wall. Other parameters are chosen identically as in Fig. 6, as are symbols and color codes.
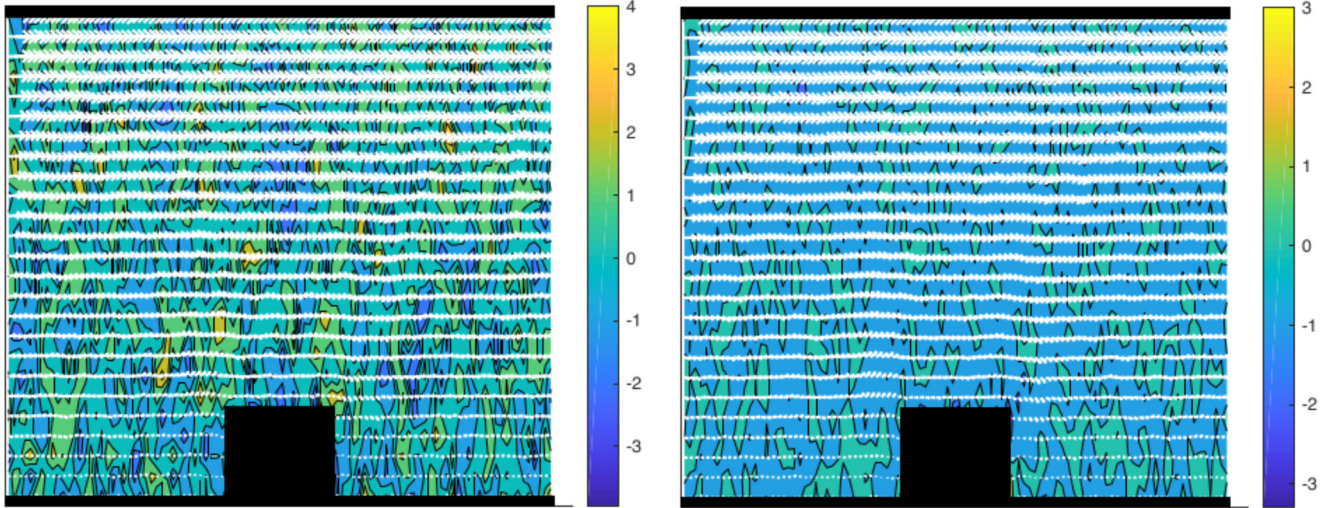
FIG. 8. Shear flow over obstacle with white arrows indicating the flow field. Color codes (in units 10^{-3}) indicate the local nonequilibrium magnetization component M_x/M_{sat} and M_y/M_{sat} when an external field of strength $h_0 = 2$ is applied in gradient (left panel) and flow direction (right panel), respectively.

errors for M_x are more pronounced than for the velocity field, probably due to the smallness of the nonequilibrium magnetization component and numerical uncertainties due the moderate number $Q = 30$ of particles per cell.

VI. SHEAR FLOW OVER ROUGH WALLS

As a last application of the MPC model for ferrofluids, we consider shear flow over rough surfaces. Considering a planar channel geometry, shear flow is induced by the top plate moving in the x direction with a constant prescribed velocity V_{wall}. On the resting bottom plate, a rectangular ridge of width ℓ_x, height ℓ_y, and depth L_z is placed that acts as an obstacle to fluid flow, where we apply the same (no-slip) bounce back conditions on the surface of the ridge as we do on the top and bottom plate. We consider the full three-dimensional flow problem and apply periodic boundary conditions in flow (x) and neutral (z) direction. This geometry resembles patterned surfaces that are used, e.g., in microfluidic devices [47].

We simulated different channel geometries, but results will be shown for channels of size $L_x = 100$, $L_y = 25$, $L_z = 5$. The dimension of the obstacle are $\ell_x = 20$, $\ell_y = 5$. For wall velocity $V_{\text{wall}} = 0.01$ and time step $\Delta t = 0.1$, we run the simulations for 1000 integration steps to reach steady state and collect averages over the subsequent 5×10^4 steps. White arrows in Fig. 8 show the time-averaged flow field in the xy plane. For this simulation, parameters were chosen as $Q = 100$, $\tau_{\text{B}}^* = 10$, $T = 0.02$, $n^* = 0.005$, and $\chi_{\text{L}} = 2$. An external magnetic field of strength $h_0 = 2$ was applied in gradient and flow direction, respectively. Far above the obstacle, we observe a linear flow profile that is characteristic of planar Couette flow. Distortions of the flow field remain located near the obstacle and do not propagate significantly into the upper half of the channel. Such laminar flow is expected since the Reynolds number for this flow is low, $\text{Re} = V_{\text{wall}}L_y/\nu \approx 0.8$.

Although the flow fields are very similar when the external field is oriented in flow and gradient directions, the local nonequilibrium magnetization components are rather

different, as can be seen from Fig. 8. Note that in the nonequilibrium steady state for planar shear flow, the perpendicular magnetization component is proportional to the shear rate. It is interesting to note that the presence of obstacles and fluctuations lead to nonuniform and fluctuating perpendicular magnetization components, that are typically stronger when the field is oriented in gradient—compared to the flow direction.

VII. CONCLUSIONS

We here presented an implementation of fluctuating ferrohydrodynamics in terms of a hybrid simulation scheme, combining angular momentum-conserving MPC algorithm and Brownian dynamics simulations of the chain model of ferrofluids. Thereby, we modeled ferrofluids on a coarse-grained level, where each MPC particle corresponds to a small volume of fluid containing several MNPs. While previous studies [29] were restricted to the ultradilute regime, the present paper is more general and applies also to real, interacting ferrofluids with a finite concentration of MNPs. Similar to the CONNFFESSIT approach, no closed-form constitutive equations are needed here, since the Brownian dynamics simulations directly solve the stochastic magnetization dynamics, thereby avoiding closure approximations. Due to the finite ensemble size, the numerical scheme naturally includes fluctuations in the magnetization and resulting stresses. Gradients of the stress tensor act as additional forcing terms in the hydrodynamic momentum balance, whereas gradients in the velocity fields enter the magnetization dynamics. This two-way coupling of both methods ensures backflow effects are fully accounted for.

We tested and verified the implementation in several ways, successfully comparing the numerical results with theoretical predictions. The shear viscosity inferred from Poiseuille flow is very well described by the EFA for the chain model for different strengths and directions of the applied field. As an application involving nonsteady flows, we studied Stokes

second flow problem for ferrofluids. For weak amplitudes of oscillation and low enough frequencies, the resulting oscillating flow profile is well described by the theoretical result for Newtonian fluids when evaluated with the corresponding, field-dependent viscosity. We also find that the profiles of the flow-induced nonequilibrium magnetization component can be predicted rather accurately by the nonequilibrium steady-state values, when evaluated with the instantaneous local velocity gradient.

The simulation method for ferrofluids proposed here benefits from all the advantages of the MPC approach as a flexible, mesoscale simulation scheme that includes thermal fluctuations. Therefore, it is very natural to combine MPC with Brownian dynamics simulations of ferrofluid dynamics, which also includes fluctuations in the local magnetization and resulting stresses. As a solver for fluctuating ferrohydrodynamics, the hybrid scheme scheme can be applied to a wide range of flow problems. As a mesoscale method, the proposed hybrid scheme is particularly promising to study nano- and microfluidic flow problems. Similarly, small-scale boundary layer effects can be investigated with this method that are found to be relevant in blood flow [48] and presumably also in a range of biomedical applications. This approach might also be extended to explicitly include the fluid spin angular momentum balance, which would allow to study the spin-up flow in rotating magnetic fields.

APPENDIX A: CHAIN MODEL

The nth order alignment tensors are defined as the expectation value of the n-fold dyadic product of the three-dimensional unit vector **u** representing the orientation of the magnetic moment. Thus, the lowest order tensors are given by $\mathbf{A}^{(2)} = \langle \mathbf{uu} \rangle$, $\mathbf{A}^{(3)} = \langle \mathbf{uuu} \rangle$, $\mathbf{A}^{(4)} = \langle \mathbf{uuuu} \rangle$ with $\mathbf{A}^{(1)} = \langle \mathbf{u} \rangle = \mathbf{m}$ the reduced magnetization.

The geometry factors Q_i used in Sec. II depend only on the axis ratio r of the ellipsoidal aggregate. Their explicit expressions can be found in Refs. [43,44]. For ease of notation, we additionally defined the combinations

$$Q_4 = 2Q_3 - BQ_0, \tag{A1}$$

$$Q_5 = Q_{23} - 2BQ_0. \tag{A2}$$

Define the change of the dimensionless kinematic viscosity due to an applied field as $\Delta \nu_i^*(h) = \nu_i^*(h) - \nu_0^*$. When the magnetic field is oriented in the z direction, the viscosity change can be expressed as [43]

$$\Delta \nu_3^*(h) = \nu_s^* \phi \left\{ Q_2 \left[1 - 15 \frac{L_2(h)}{h^2} \right] + 2Q_3 \left[5 \frac{L_1(h)}{h} \right.\right.$$
$$\left.\left. - 10 \frac{L_2(h)}{h^2} - 1 \right] \right\}. \tag{A3}$$

It is easily verified that $\Delta \nu_3^*(h = 0) = 0$. If the magnetic field is oriented in flow direction, we get

$$\Delta \nu_1^*(h) = \Delta \nu_3^*(h) + 5\nu_s^* \phi \left\{ Q_3 \left[L_2(h) - 4 \frac{L_3(h)}{h} \right] - 3Q_2 \frac{L_3(h)}{h} \right.$$
$$\left. - \frac{1}{2} Q_0 L_2(h) \right\} + \frac{3}{2} \nu_s^* \phi \frac{h L_1^2(h)}{h - L_1(h)} (1 - B\alpha(h)), \tag{A4}$$

while for the case that the field is oriented in the gradient (y) direction,

$$\Delta \nu_2^*(h) = \Delta \nu_3^*(h) + 5\nu_s^* \phi \left\{ Q_3 \left[L_2(h) - 4 \frac{L_3(h)}{h} \right] - 3Q_2 \frac{L_3(h)}{h} \right.$$
$$\left. + \frac{1}{2} Q_0 L_2(h) \right\} + \frac{3}{2} \nu_s^* \phi \frac{h L_1^2(h)}{h - L_1(h)} (1 + B\alpha(h)), \tag{A5}$$

where $\alpha(h) = 1 - 2L_2(h)/[hL_1(h)]$. These expressions can also be inferred from Ref. [44].

In the limit of spherical particles, $r = 1$ leading to $B = Q_0 = Q_2 = Q_3 = 0$, and we recover $\nu_1 = \nu_2$ and $\Delta \nu_3 = 0$ valid for noninteracting ferrofluids. The difference between ν_1 and ν_2 as well as the field dependence of the viscosity coefficient ν_3 are hallmarks of interacting ferrofluids that are captured by the chain model ($r \neq 1$).

APPENDIX B: FERROHYDRODYNAMIC MPC ALGORITHM

Here, we summarize the algorithm to implement the hybrid ferrohydrodynamic MPC model described in Sec. III. Integrating this model over the time interval Δt involves steps 1–7 shown in Table I.

APPENDIX C: STOKES SECOND FLOW PROBLEM FOR FERROFLUIDS

Using the ansatz $\mathbf{v} = (v_x(y, t), 0, 0)$ for the laminar velocity profile, the momentum balance Eq. (1) becomes

$$\frac{\partial v_x}{\partial t} = \frac{1}{\rho} \frac{\partial \sigma_{yx}^{\mathrm{hyd}}}{\partial y} + f_{\mathbf{M},x}. \tag{C1}$$

The stress contributions (4) and (5) to $\sigma_{yx}^{\mathrm{hyd}}$ become

$$T_{yx}^{\mathrm{vis}} = \left(1 + \frac{5}{2} \phi \left[2Q_1 + Q_4(A_{xx}^{(2)} + A_{yy}^{(2)}) - 2Q_5 A_{xxyy}^{(4)} \right] \right) \eta_s \frac{\partial v_x}{\partial y} \tag{C2}$$

and

$$T_{yx}^{\mathrm{pot}} = \frac{1}{2} n k_{\mathrm{B}} T B \left[6A_{xy}^{(2)} - (m_x h_y + m_y h_x) + A_{xxy}^{(3)} h_x + A_{xyy}^{(3)} h_y \right]. \tag{C3}$$

In the last term, we assumed $h_z = 0$, i.e., the magnetic field has no component in the z direction. Finally, for the Kelvin-Helmholtz force density (2), we find

$$\rho f_{\mathbf{M},x} = \frac{1}{2} n k_{\mathrm{B}} T \left(h_y \frac{\partial m_x}{\partial y} - h_x \frac{\partial m_y}{\partial y} + m_x \frac{\partial h_y}{\partial y} \right). \tag{C4}$$

TABLE I. Algorithm to implement the hybrid MPC–Brownian dynamics algorithm for fluctuating ferrohydrodynamics.

Hybrid MPC–Brownian dynamics algorithm
1: Cell-level calculation of the magnetization $\mathbf{m}_{C_i}$ and local magnetic field $\mathbf{h}_{C_i}$ as well as $\mathbf{A}_{C_i}^{(k)}$ for $k = 2, 3, 4$.
2: Use finite-difference approximations to calculate the force (9) from (2) and the divergence of (4) and (5).
3: Streaming step: Update particle positions and velocities according to Eqs. (7) and (8) for a time step Δt.
4: Apply (periodic or bounce-back) boundary conditions.
5: Use finite-difference approximation to calculate the cell-level vorticity $\mathbf{\Omega}_{C_i}$ and symmetric velocity gradient $\mathbf{D}_{C_i}$.
6: Perform n_{BD} time steps Brownian dynamics simulation of Eq. (12) with time step $\Delta t / n_{\mathrm{BD}}$.
7: Collisions: Apply the Andersen-AT+a thermostat (10).

In first-order perturbation for weak velocity gradients, the coefficients $A^{(2)}$ and $A^{(4)}$ in (C2) can be replaced by their equilibrium values,

$$A_{xx,\mathrm{eq}}^{(2)} = \langle u_x^2 \rangle_{\mathrm{eq}} = L_2(h)\hat{h}_x^2 + \frac{L_1(h)}{h}, \qquad \text{(C5)}$$

where $\hat{\mathbf{h}}$ denotes the unit vector in the direction of the magnetic field and $L_2(h) = 1 - 3L_1(h)/h$. The corresponding expression for $A^{(4)}$ can, e.g., be found in Ref. [44].

In the absence of an external field, we find $A_{xx,\mathrm{eq}}^{(2)} = A_{xx,\mathrm{eq}}^{(2)} = 1/3$ and $A_{xxyy,\mathrm{eq}}^{(4)} = 1/15$. In this case, the contribution (C4) vanishes and (C3) simplifies to $3nk_{\mathrm{B}}TBA_{xy}^{(2)}$. Calculating this quantity to first order in the velocity gradient [43], we find from (C2) the resulting zero-field viscosity $\eta_0 = (1 + c_r\phi)\eta_s$ with $c_r = 5Q_1 + 2Q_3 - Q_2$ given in Sec. IV. Evaluating the expressions (C2)–(C4) in the presence of an external field is more involved. The corresponding calculations within the EFA can be found in Refs. [43,44]. In the special case of spa-tially homogeneous magnetic field and magnetization, we find that Eq. (16) reduces to (17) with the viscosity coefficients (A3)–(A5).

Within the EFA, the magnetization component in flow direction for a field applied in the gradient direction was obtained in Ref. [43] as

$$M_x/M_{\mathrm{sat}} = \tau_{\mathrm{B}}\dot{\gamma}\frac{L_1^2(h)}{h - L_1(h)}(1 + B\alpha(h)), \qquad \text{(C6)}$$

where $\alpha(h)$ is defined in Appendix A.

Assuming that the amplitude U_0 of the oscillating plate is small enough to remain in the linear flow regime and the frequency ω to be low enough to be considered as quasistatic, we can approximate the profile $M_x(y, t)$ by Eq. (C6) with the instantaneous local shear rate $\dot{\gamma} = \dot{\gamma}(y, t)$:

$$\dot{\gamma}(y, t) = \frac{\partial v_x(y, t)}{\partial y} = -\sqrt{2}\,kU_0 e^{-ky}\cos(\omega t - ky + \pi/4).$$

$$\text{(C7)}$$

[1] D. Ghosh and P. K. Das, Phys. Fluids **31**, 083609 (2019).

[2] S. Odenbach, ed., *Ferrofluids. Magnetically Controllable Fluids and Their Applications*, Lecture Notes in Phys. (Springer, Berlin, 2002), Vol. 594

[3] I. Torres-Díaz and C. Rinaldi, Soft Matter **10**, 8584 (2014).

[4] A. Munaz, M. J. A. Shiddiky, and N.-T. Nguyen, Biomicrofluidics **12**, 031501 (2018).

[5] F. Wiekhorst, U. Steinhoff, D. Eberbeck, and L. Trahms, Pharm. Res. **29**, 1189 (2012).

[6] H. Ye, Z. Shen, L. Yu, M. Wei, and Y. Li, Proc. R. Soc. A. **474**, 20170845 (2018).

[7] L. J. Felicia, S. Vinod, and J. Philip, J. Nanofluids **5**, 1 (2016).

[8] V. Socoliuc, M. V. Avdeev, V. Kuncser, R. Turcu, E. Tombácz, and L. Vékás, Nanoscale **14**, 4786 (2022).

[9] R. E. Rosensweig, *Ferrohydrodynamics* (Cambridge University Press, Cambridge, 1985).

[10] M. Liu and K. Stierstadt, in *Colloidal Magnetic Fluids: Basics, Development and Applications of Ferrofluids*, Lecture Notes in Physics, edited by S. Odenbach (Springer, Berlin, 2008), Vol. 763.

[11] B. U. Felderhof and H. J. Kroh, J. Chem. Phys. **110**, 7403 (1999).

[12] M. I. Shliomis, in *Ferrofluids. Magnetically Controllable Fluids and Their Applications*, Lecture Notes in Physics, edited by S. Odenbach (Springer, Berlin, 2002), Vol. 594, pp. 85–111.

[13] M. A. Martsenyuk, Y. L. Raikher, and M. I. Shliomis, Sov. Phys. J. Exp. Theor. Phys. **38**, 413 (1974).

[14] A. Y. Zubarev and L. Y. Iskakova, Sov. Phys. J. Exp. Theor. Phys. **80**, 857 (1995).

[15] A. Y. Zubarev and L. Y. Iskakova, Phys. Rev. E **61**, 5415 (2000).

[16] P. Ilg and S. Odenbach, in *Colloidal Magnetic Fluids: Basics, Development and Applications of Ferrofluids*, Lecture Notes in Physics, edited by S. Odenbach (Springer, Berlin, 2008), Vol. 763.

[17] A. Fang, Phys. Fluids **34**, 013319 (2022).

[18] M. I. Shliomis, Phys. Fluids **34**, 079101 (2022).

[19] A. Leschhorn and M. Lücke, Z. Phys. Chem. **220**, 219 (2006).

[20] S. Odenbach and H. W. Müller, Phys. Rev. Lett. **89**, 037202 (2002).

[21] P. Ilg, M. Kröger, and S. Hess, Phys. Rev. E **71**, 031205 (2005).

[22] P. Ilg, E. Coquelle, and S. Hess, J. Phys.: Condens. Matter **18**, S2757 (2006).

[23] S. Altmeyer, Sci. Rep. **11**, 4705 (2021).

[24] S. Kayal, D. Bandyopadhyay, T. K. Mandal, and R. V. Ramanujan, RSC Adv. **1**, 238 (2011).

[25] F. Selimefendigil and H. F. Öztop, Eng. Sci. Technol. **18**, 439 (2015).

[26] M. Sheikholeslami, M. Barzegar Gerdroodbary, S. V. Mousavi, D. D. Ganji, and R. Moradi, J. Magn. Magn. Mater. **460**, 302 (2018).

[27] C. Singh, A. K. Das, and P. K. Das, Phys. Fluids **28**, 087103 (2016).

[28] C. Alegretti and R. Gontijo, J. Magn. Magn. Mater. **514**, 167133 (2020).

[29] P. Ilg, J. Chem. Phys. **156**, 144905 (2022).

[30] A. Malevanets and R. Kapral, J. Chem. Phys. **110**, 8605 (1999).

[31] T. Ihle and D. M. Kroll, Phys. Rev. E **63**, 020201(R) (2001).

[32] G. Gompper, T. Ihle, D. M. Kroll, and R. G. Winkler, Advanced Computer Simulation Approaches For Soft Matter Sciences III **221**, 1 (2009).

[33] D. Zablotsky, J. Magn. Magn. Mater. **474**, 462 (2019).

[34] B. Kowalik and R. G. Winkler, J. Chem. Phys. **138**, 104903 (2013).

[35] S. Mandal and M. G. Mazza, Phys. Rev. E **99**, 063319 (2019).

[36] M. Laso and H. Öttinger, J. Non-Newtonian Fluid Mech. **47**, 1 (1993).

[37] M. Gerth-Noritzsch, D. Y. Borin, and S. Odenbach, J. Phys.: Condens. Matter **23**, 346002 (2011).

[38] A. Sreekumari and P. Ilg, Phys. Rev. E **92**, 012306 (2015).

[39] F. R. Cunha, Y. Z. Sinzato, and I. D. O. Pereira, Phys. Fluids **34**, 093314 (2022).

[40] A. Y. Zubarev, S. Odenbach, and J. Fleischer, J. Magn. Magn. Mater. **252**, 241 (2002).

[41] E. De Angelis, M. Chinappi, and G. Graziani, Meccanica **47**, 2069 (2012).

[42] M. Kröger and H. S. Sellers, J. Chem. Phys. **103**, 807 (1995).

[43] P. Ilg, M. Kröger, S. Hess, and A. Y. Zubarev, Phys. Rev. E **67**, 061401 (2003).

[44] P. Ilg and M. Kröger, Phys. Rev. E **66**, 021501 (2002); **67**, 049901(E) (2003).

[45] J. K. Whitmer and E. Erik Luijten, J. Phys.: Condens. Matter **22**, 104106 (2010).

[46] H. Noguchi and G. Gompper, Phys. Rev. E **78**, 016706 (2008).

[47] H. Suzuki, R. Hidema, and Y. Komoda, Exp. Therm. Fluid Sci. **67**, 96 (2015), Heat Transfer and Fluid Flow in Microscale.

[48] A. Nacev, C. Beni, O. Bruno, and B. Shapiro, J. Magn. Magn. Mater. **323**, 651 (2011).